Supporting Information for

Achieving Superior Oxygen Evolution Performance on Multi-cation Boride Catalysts

Junxiu Liu[1,3]*, Weiwei Li[1], Gui Wang[1], Xiaoliang Zhang[1], Meng Song[1], Hongliang Dong[1], Hongwei Sheng[1], Bin Chen[1], Yu He[2]*, Hengzhong Zhang[1]*

[1]Center for High Pressure Science and Technology Advanced Research, Shanghai 201203.

[2]Key Laboratory of High-Temperature and High-Pressure Study of the Earth's Interior, Institute of Geochemistry, Chinese Academy of Sciences, Guiyang, 550081.

[3]Shanghai Key Laboratory MFree, Shanghai Advanced Research in Physical Sciences, Shanghai 201203.

*Corresponding authors: junxiu.liu@hpstar.ac.cn; heyu@mail.gyig.ac.cn; hengzhong.zhang@hpstar.ac.cn.

Contents:

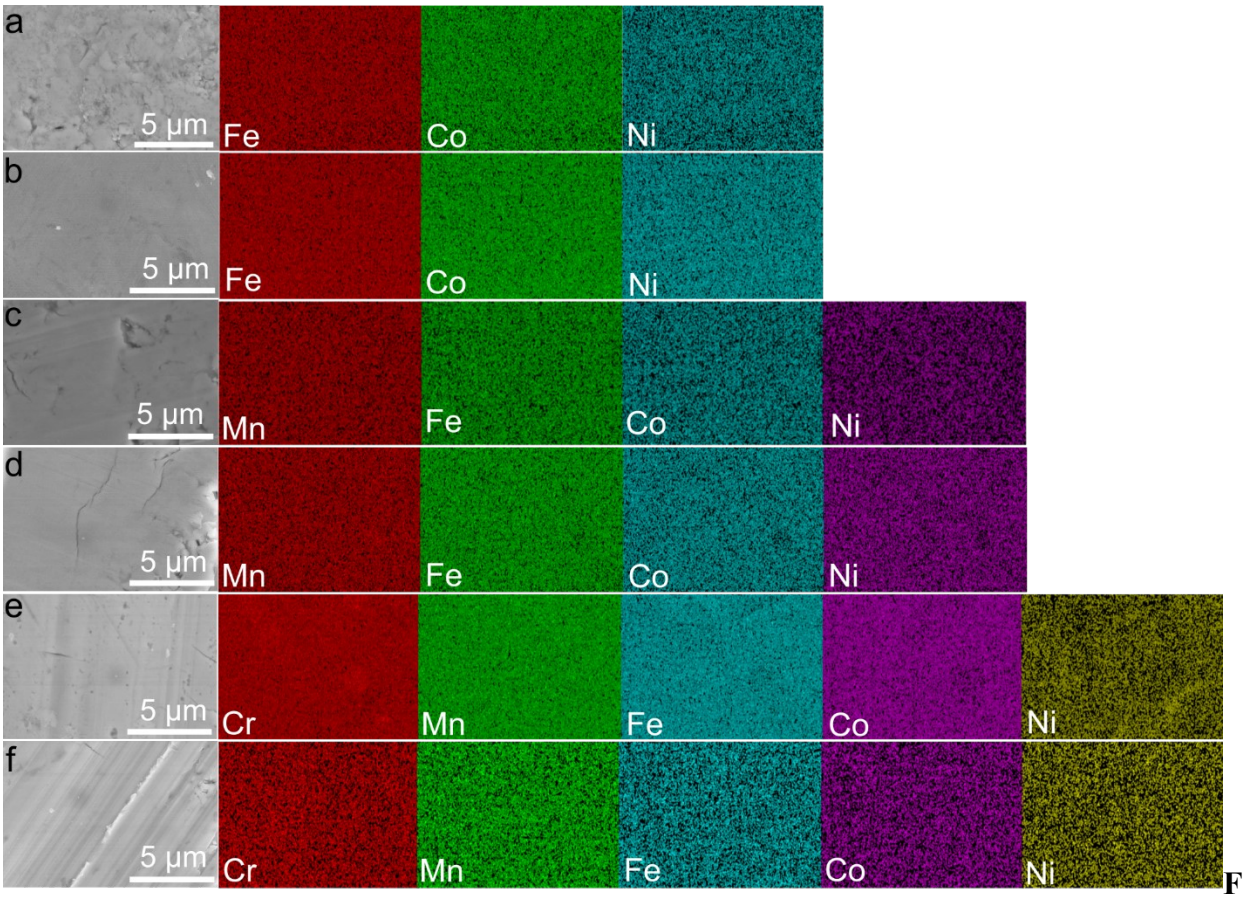

F igure S1. SEM images and EDS metal elemental mapping of the synthesized MEB/HEB catalysts. Metal elemental mapping in (FeCoNi)B (a), $(FeCoNi)_2B$ (b), (MnFeCoNi)B (c), $(MnFeCoNi)_2B$ (d), (CrMnFeCoNi)B (e), and $(CrMnFeCoNi)_2B$ (f).

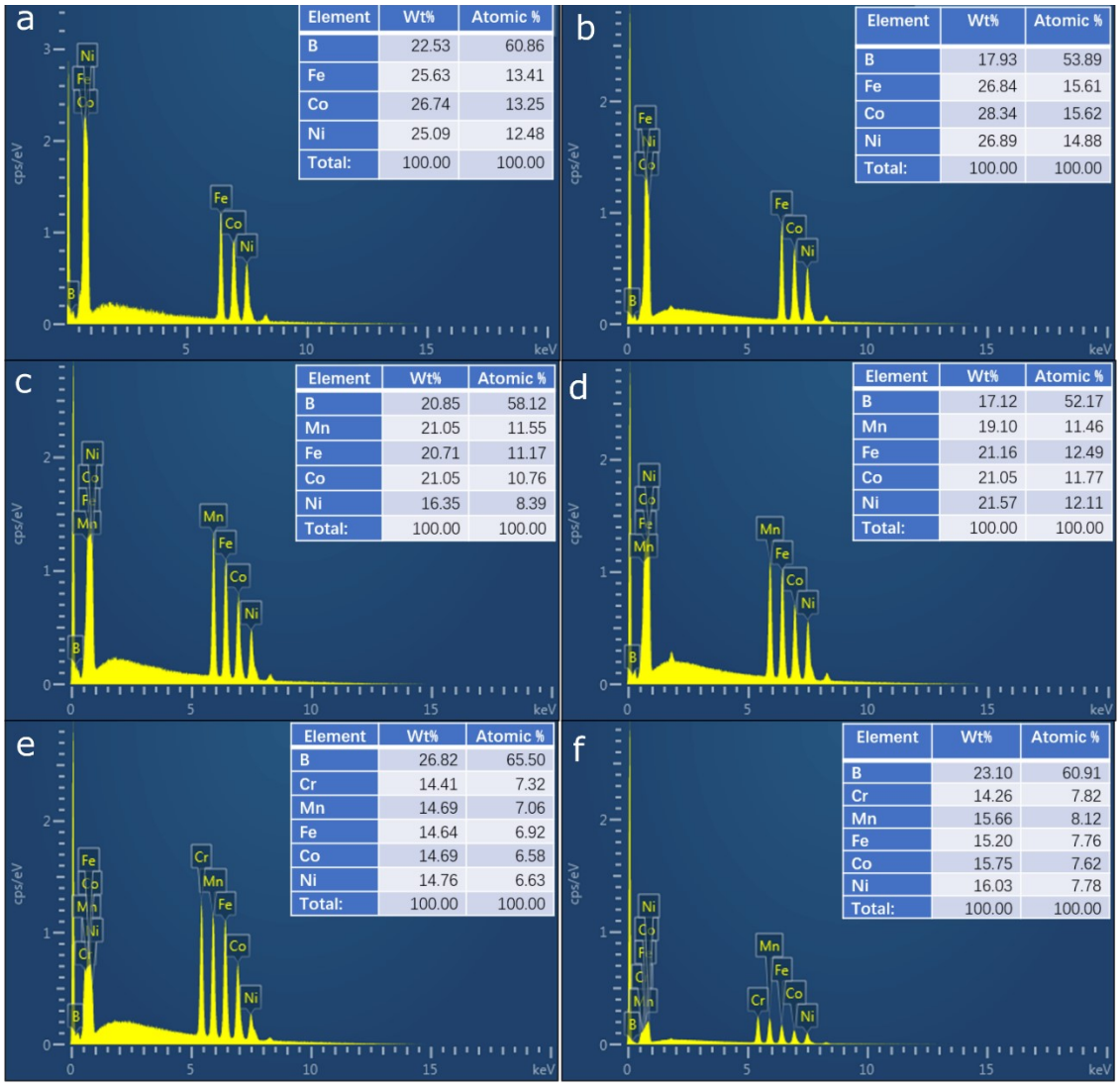

Figure S2. EDS-determined elemental contents of the synthesized MEB/HEB samples. EDS of (FeCoNi)B (a), $(FeCoNi)_2B$ (b), (MnFeCoNi)B (c), $(MnFeCoNi)_2B$ (d), (CrMnFeCoNi) (e), and $(CrMnFeCoNi)_2B$ (f).

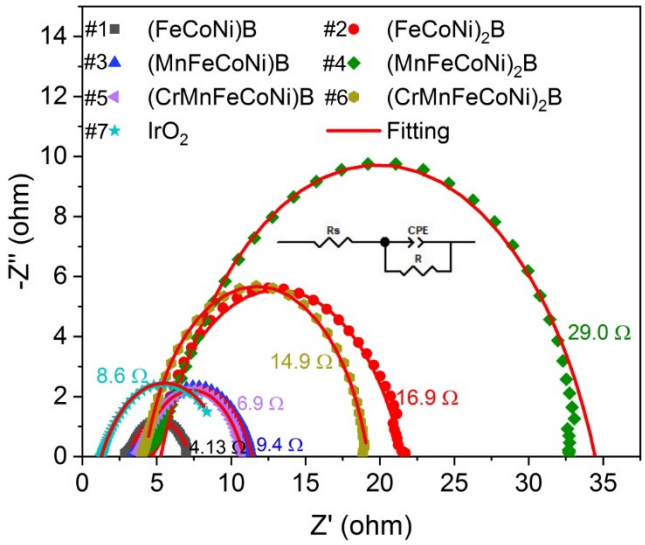

Figure S3. Nyquist plots of the MEB/HEB catalysts in bulk pieces with polished surfaces. Nyquist plots of (FeCoNi)B, $(FeCoNi)_2B$, (MnFeCoNi)B, $(MnFeCoNi)_2B$, (CrMnFeCoNi)B, $(CrMnFeCoNi)_2B$, and of the benchmark IrO_2 powders loaded on a carbon paper substrate.

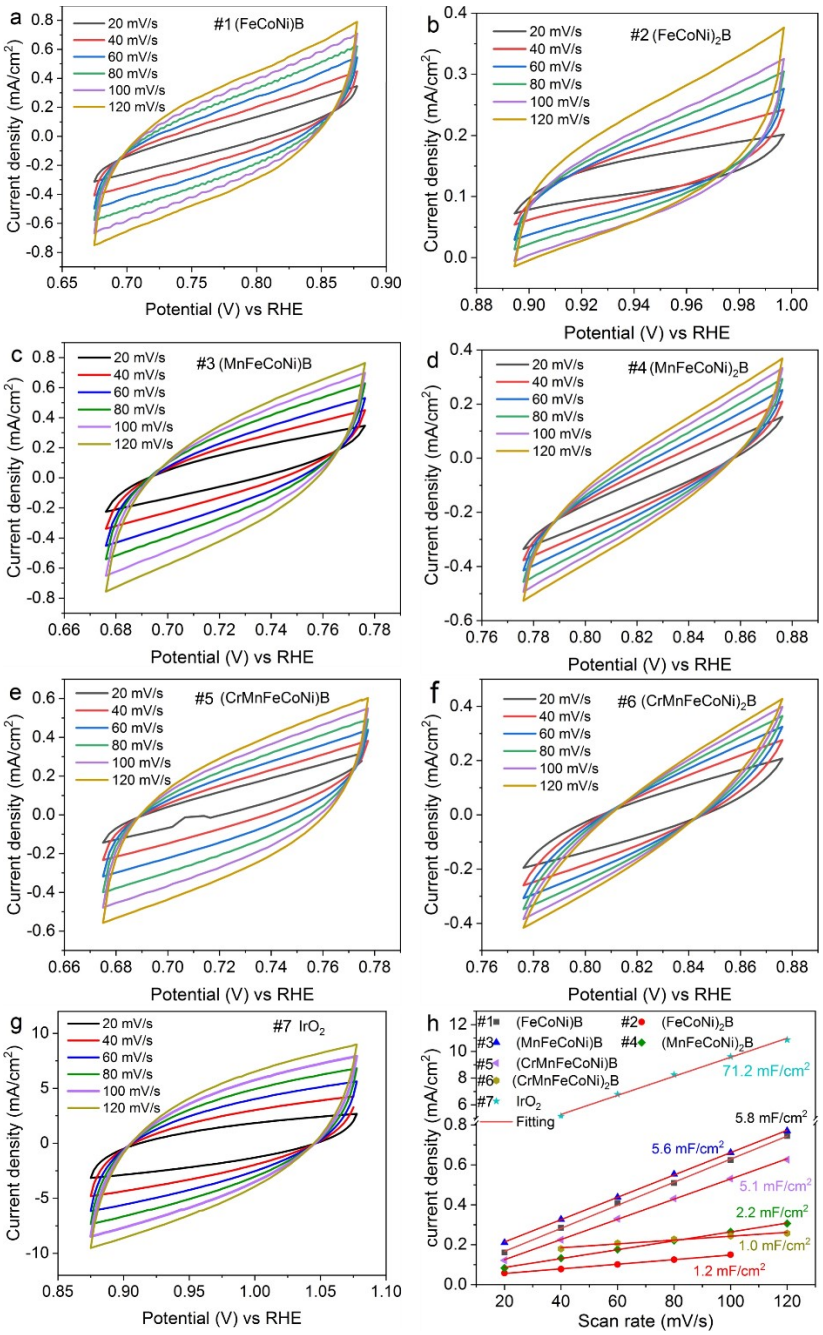

Figure S4. Cyclic voltammograms of the MEB/HEB catalysts in bulk pieces with polished surfaces. CV curves of (FeCoNi)B (a), $(FeCoNi)_2B$ (b), (MnFeCoNi)B (c), $(MnFeCoNi)_2B$ (d), (CrMnFeCoNi)B (e), $(CrMnFeCoNi)_2B$ (f), and IrO_2 (g) powders loaded on a carbon paper substrate. h), difference between anodic and cathodic current densities versus the scan rate, which

was used to derive the ECSA of the catalysts.

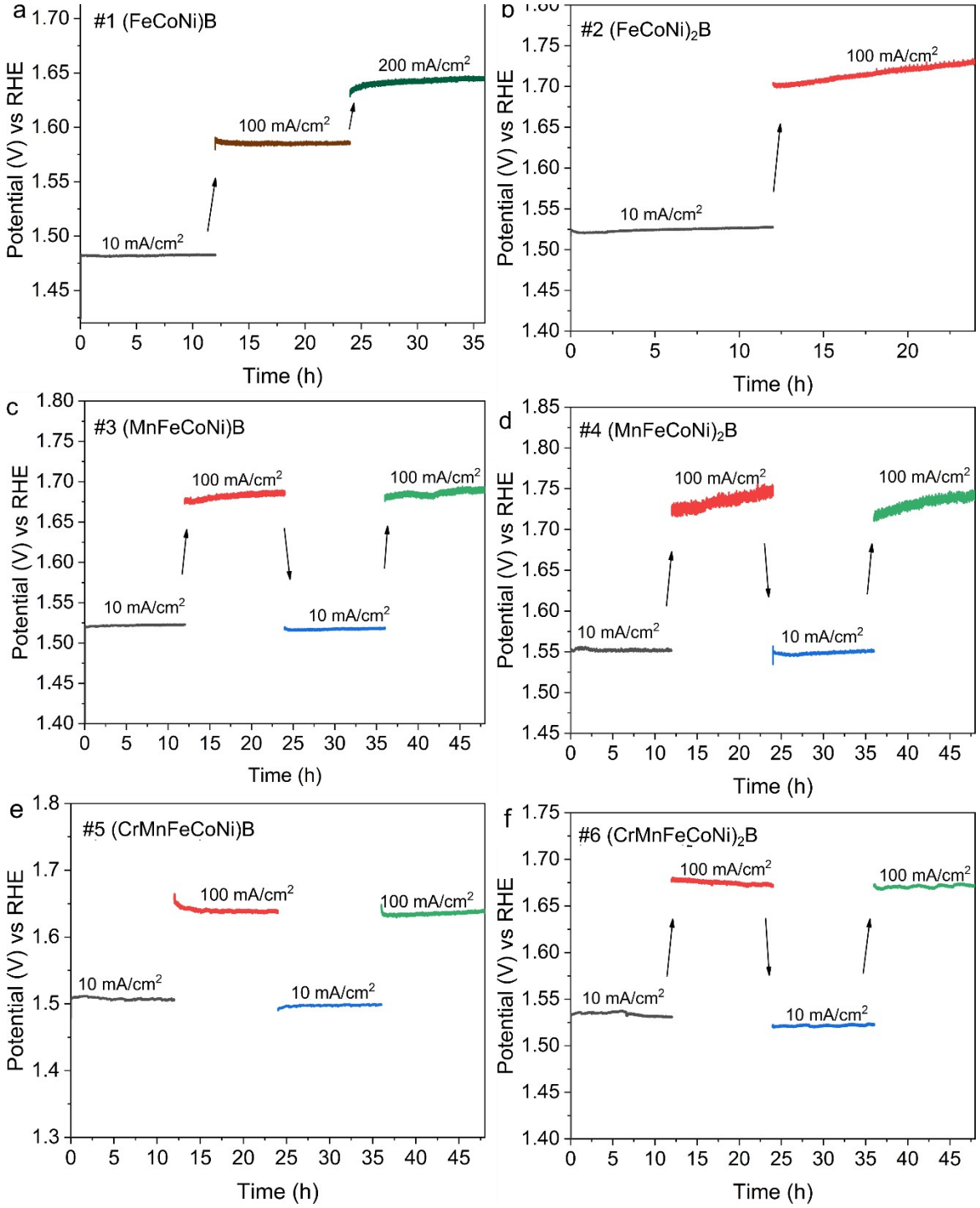

Figure S5. Chronopotentiometric curves of the MEB/HEB catalysts at a current density of 10, 100

and 200 mA cm^{-2}. Chronopotentiometric curves of (FeCoNi)B (a), $(FeCoNi)_2B$ (b), (MnFeCoNi)B (c), $(MnFeCoNi)_2B$ (d), (CrMnFeCoNi)B (e), and $(CrMnFeCoNi)_2B$ (f).

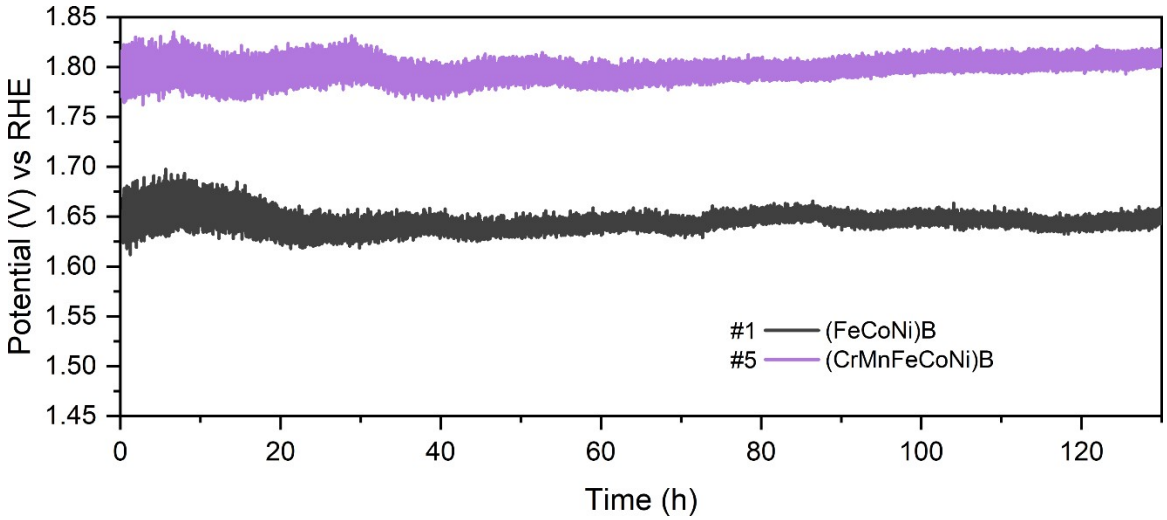

Figure S6. Chronopotentiometric curves of (FeCoNi)B and CrMnFeCoNi)B catalysts at a current density of 200 mA cm^{-2} for 130h.

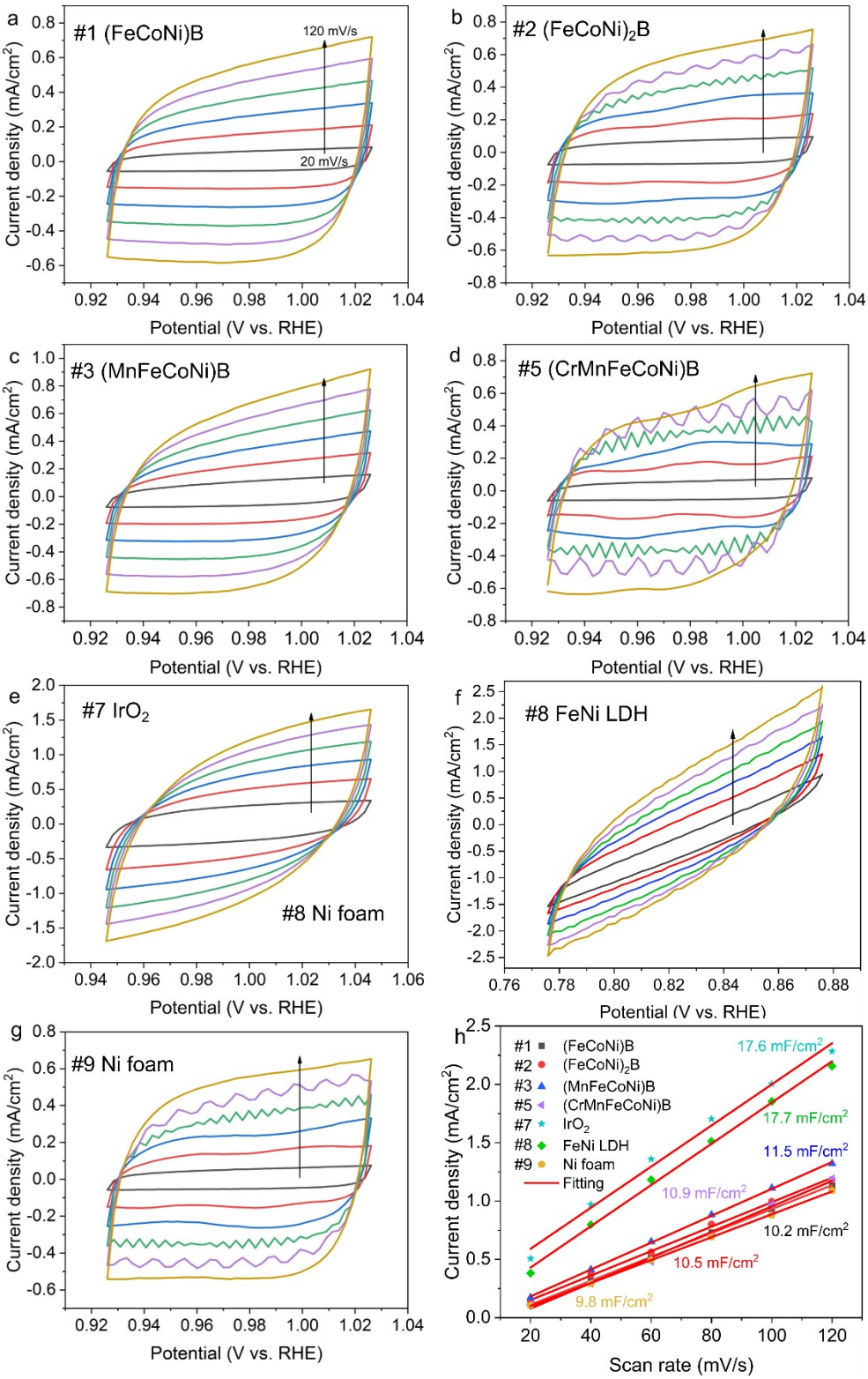

Figure S7. Cyclic voltammograms in the double layer region of powdered MEB/HEB catalysts

loaded on nickel-foam substrates. CV curves of (FeCoNi)B (a), $(FeCoNi)_2B$ (b), (MnFeCoNi)B (c), (CrMnFeCoNi)B (d), IrO_2 (e), FeNi LDH (f), and Ni foam (g). (h) difference between anodic and cathodic current densities versus the scan rate, which was used to derive the ECSA of the electrodes. The scan rate ranges from 20 to 120 mV/s at an increment of 20 mV/s, as shown in a - g along the arrow direction.

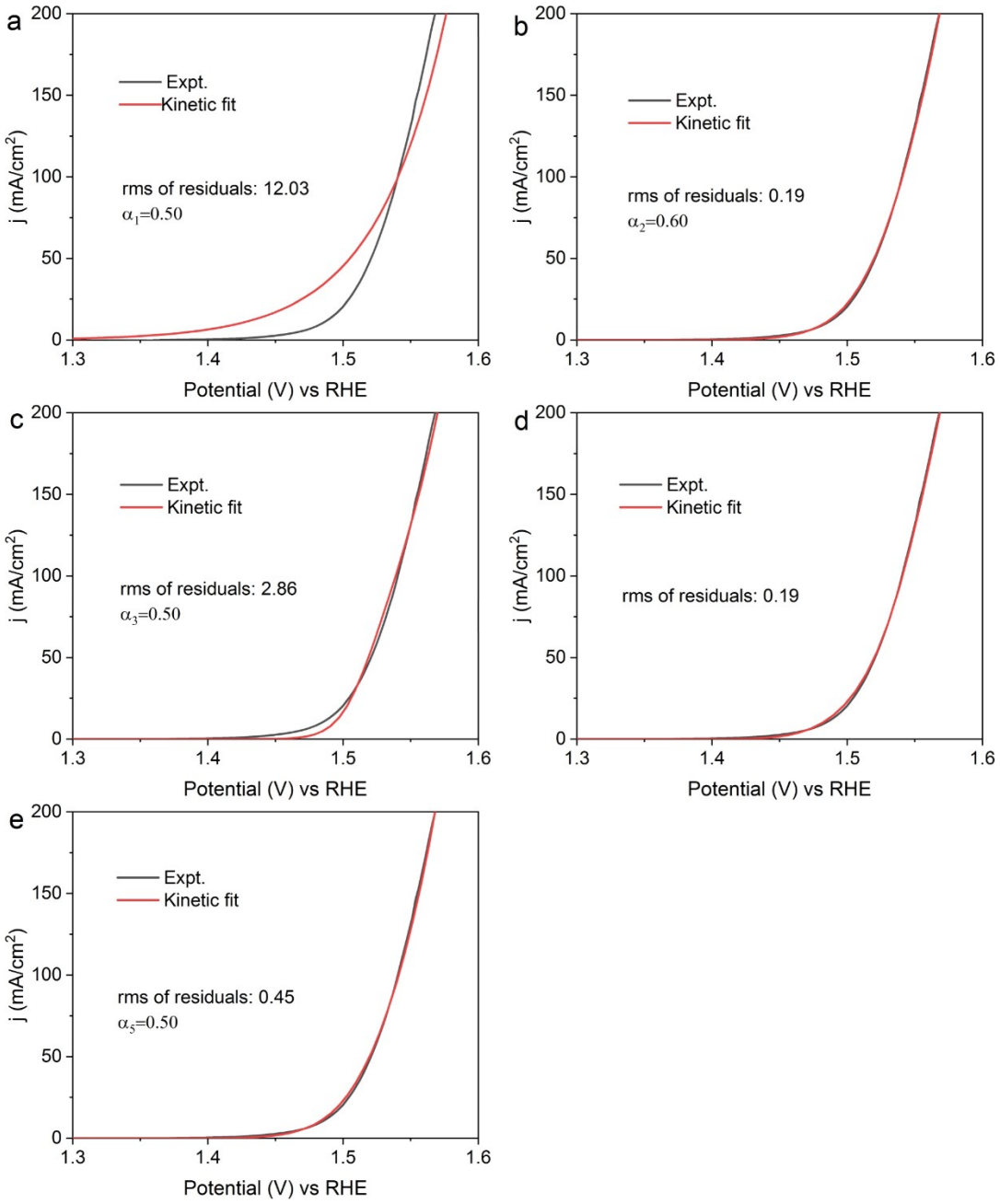

Figure S8. Microkinetic modeling. Fitting of the OER pol**a**rization curve of (FeCoNi)B (#1) using equations S1 (a), S2 (b), S3 (c), S4 (d), and S5 (e) in the Supplementary Note. α_i (i = 1, 2, 3, 5) is the electron transfer coefficient contained in equations S1, S2, S3, and/or S5.

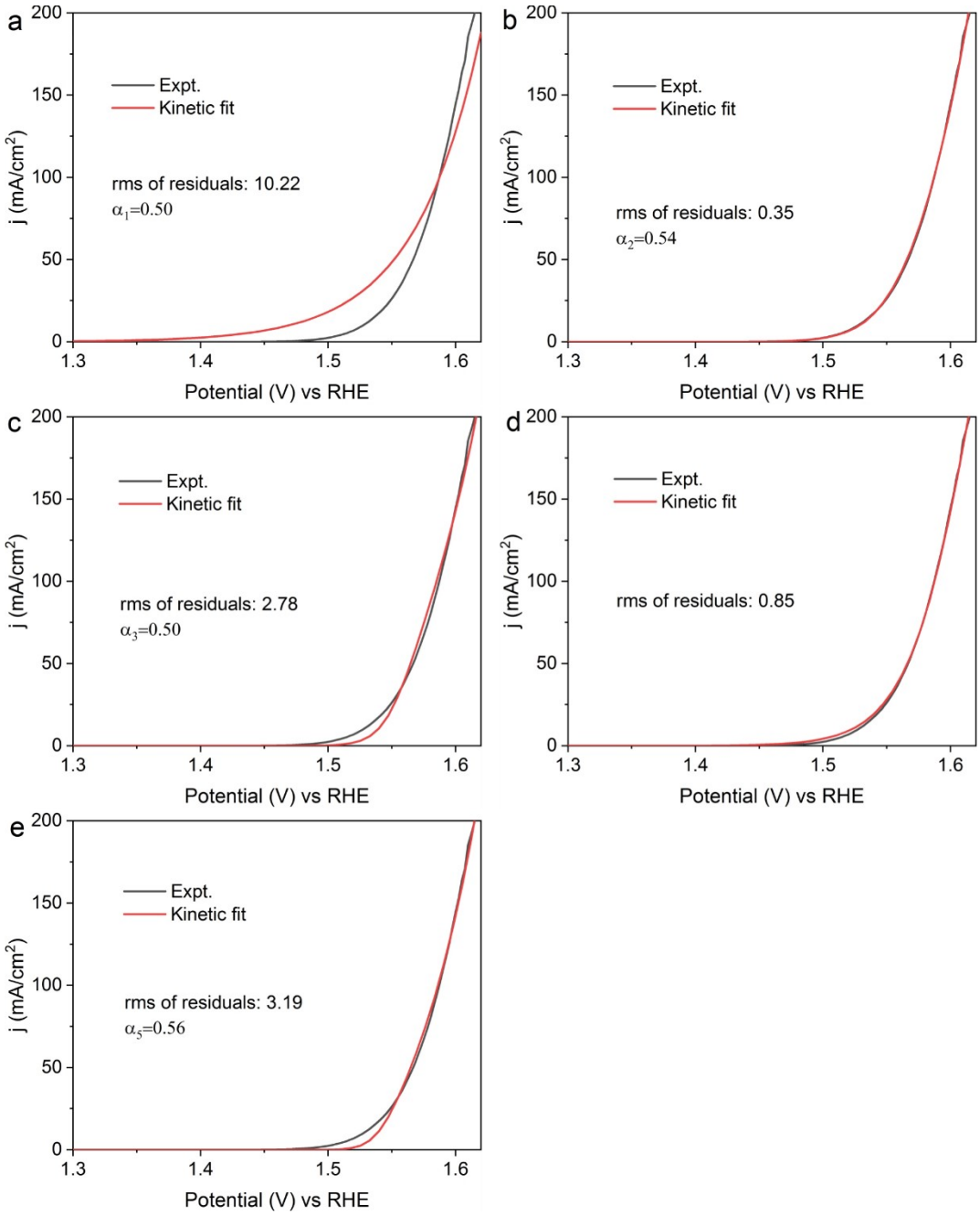

Figure S9. Microkinetic modeling. Fitting of the OER polarization curve of $(FeCoNi)_2B$ (#2) using equations S1 (a), S2 (b), S3 (c), S4 (d), and S5 (e) in the Supplementary Note. α_i (i = 1, 2, 3, 5) is the electron transfer coefficient contained in equations S1, S2, S3, and/or S5.

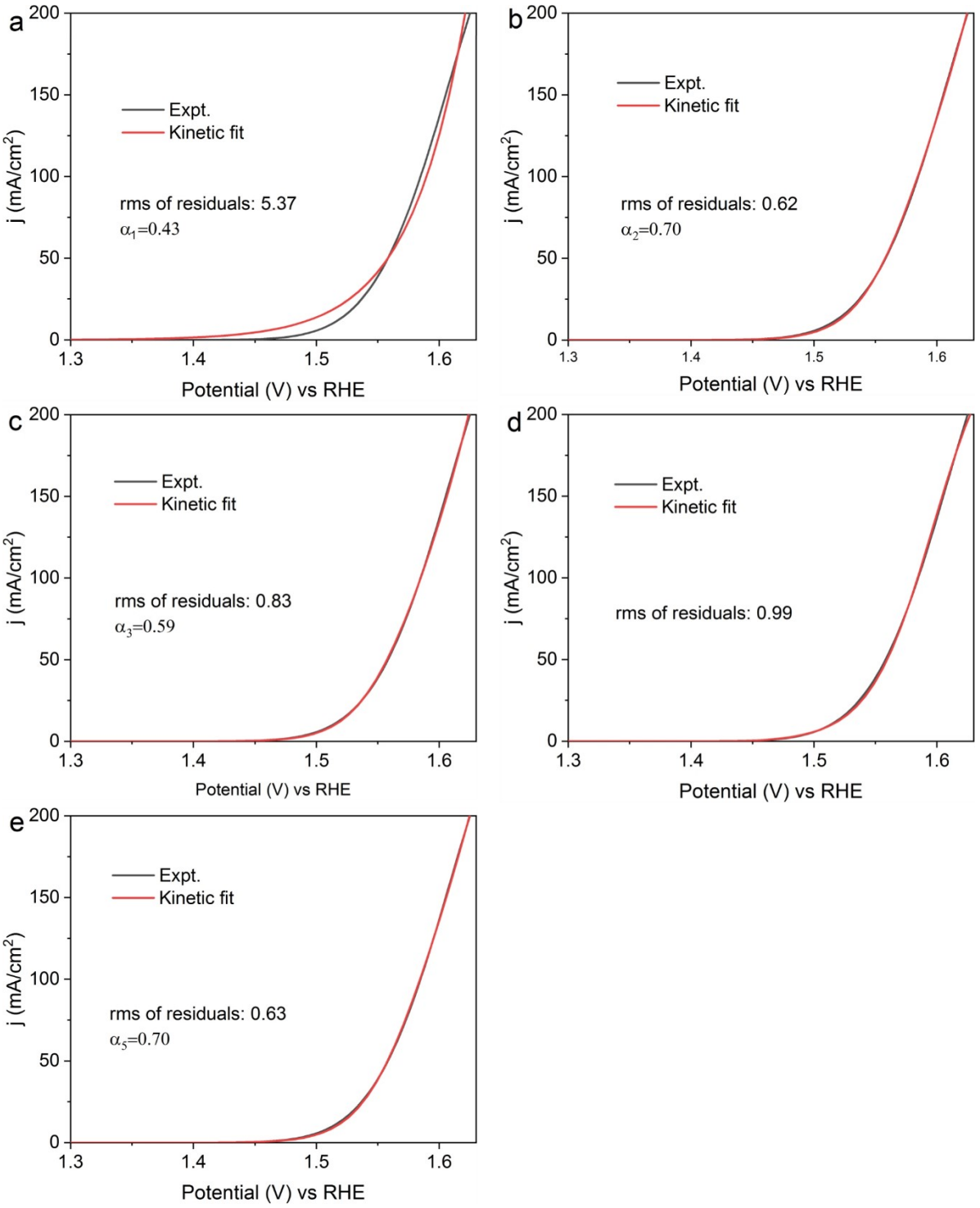

Figure S10. Microkinetic modeling. Fitting of the OER polarization curve of (MnFeCoNi)B (#3) using equations S1 (a), S2 (b), S3 (c), S4 (d), and S5 (e) in the Supplementary Note. α_i (i = 1, 2, 3,

5) is the electron transfer coefficient contained in equations S1, S2, S3, and/or S5.

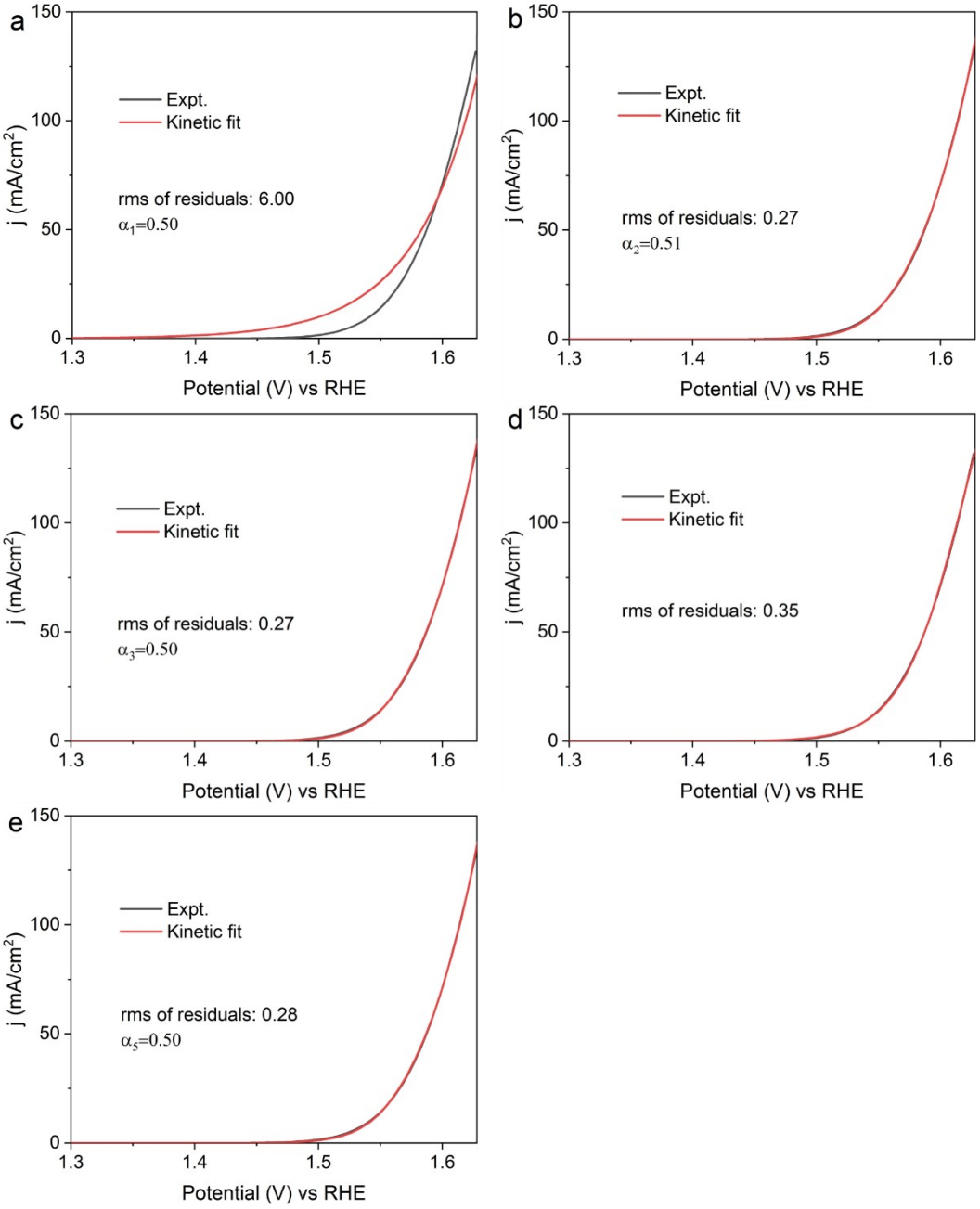

Figure S11. Microkinetic modeling. Fitting of the OER polarization curve of $(MnFeCoNi)_2B$ (#4) using equations S1 (a), S2 (b), S3 (c), S4 (d), and S5 (e) in the Supplementary Note. α_i (i = 1, 2, 3, 5) is the electron transfer coefficient contained in equations S1, S2, S3, and/or S5.

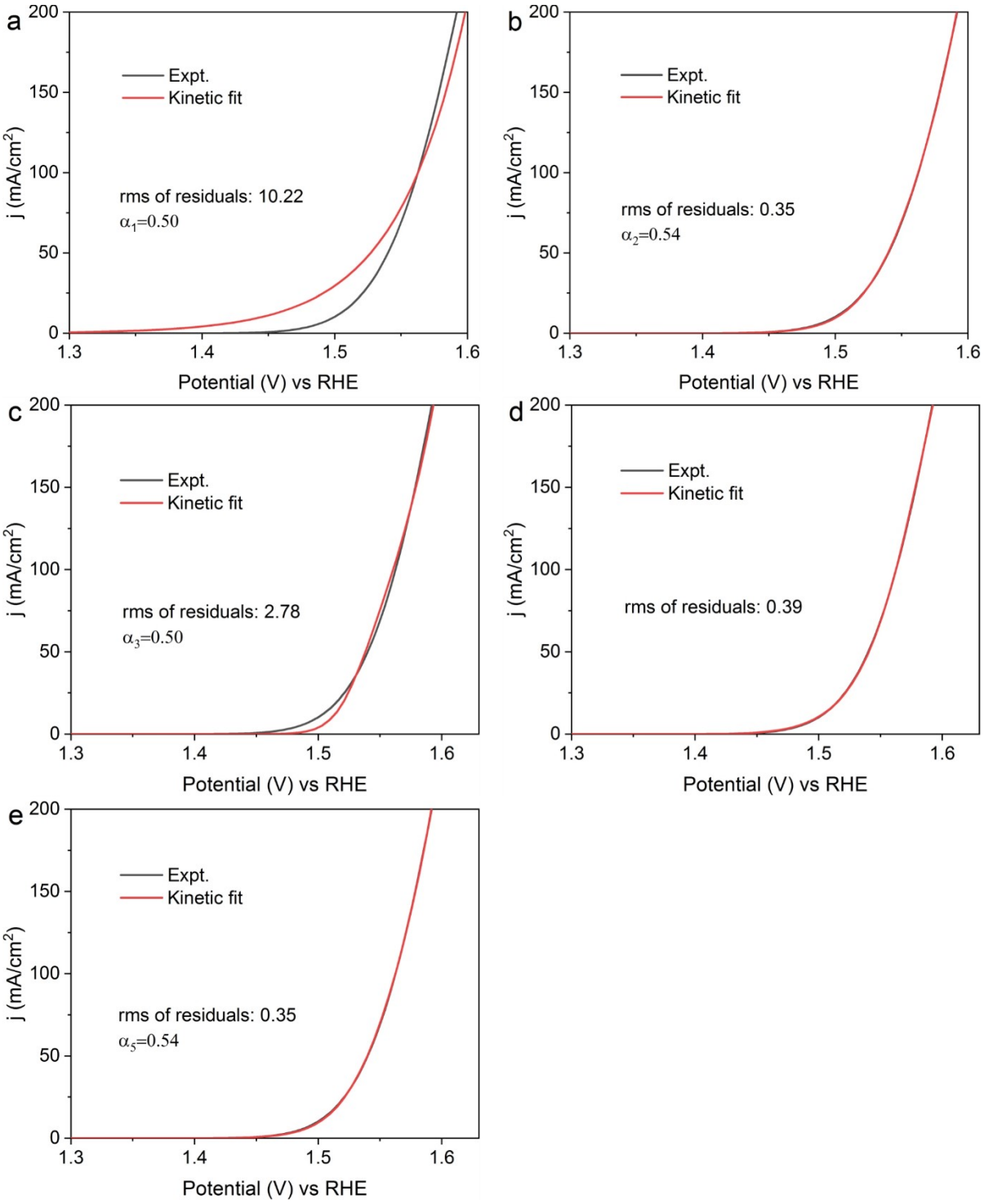

Figure S12. Microkinetic modeling. Fitting of the OER polarization curve of (CrMnFeCoNi)B (#5) using equations S1 (a), S2 (b), S3 (c), S4 (d), and S5 (e) in the Supplementary Note. α_i (i = 1,

2, 3, 5) is the electron transfer coefficient contained in equations S1, S2, S3, and/or S5.

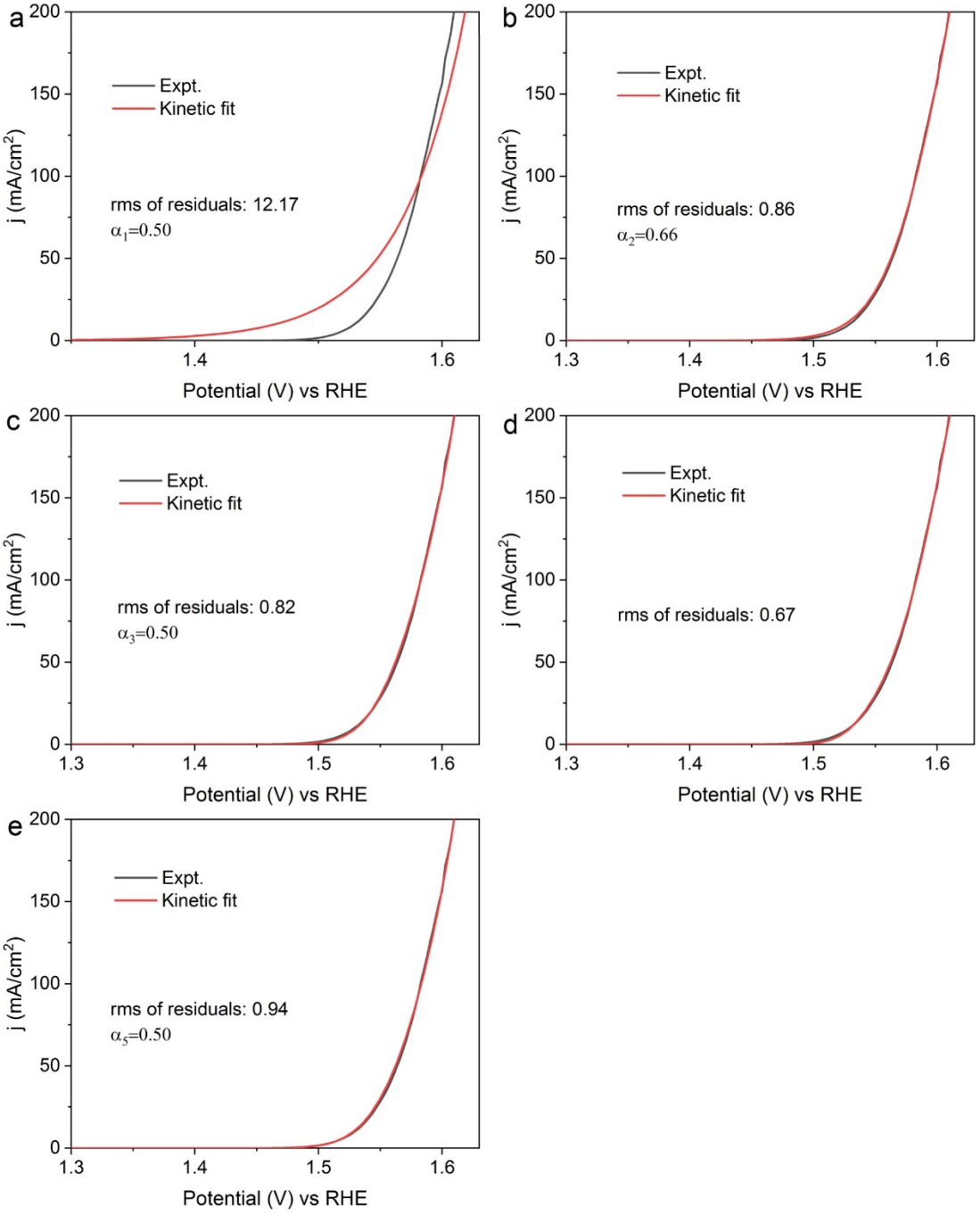

Figure S13. Microkinetic modeling. Fitting of the OER polarization curve of $(CrMnFeCoNi)_2B$ (#6) using equations S1 (a), S2 (b), S3 (c), S4(d), and S5 (e) in the Supplementary Note. α_i (i = 1,

2, 3, 5) is the electron transfer coefficient contained in equations S1, S2, S3, and/or S5.

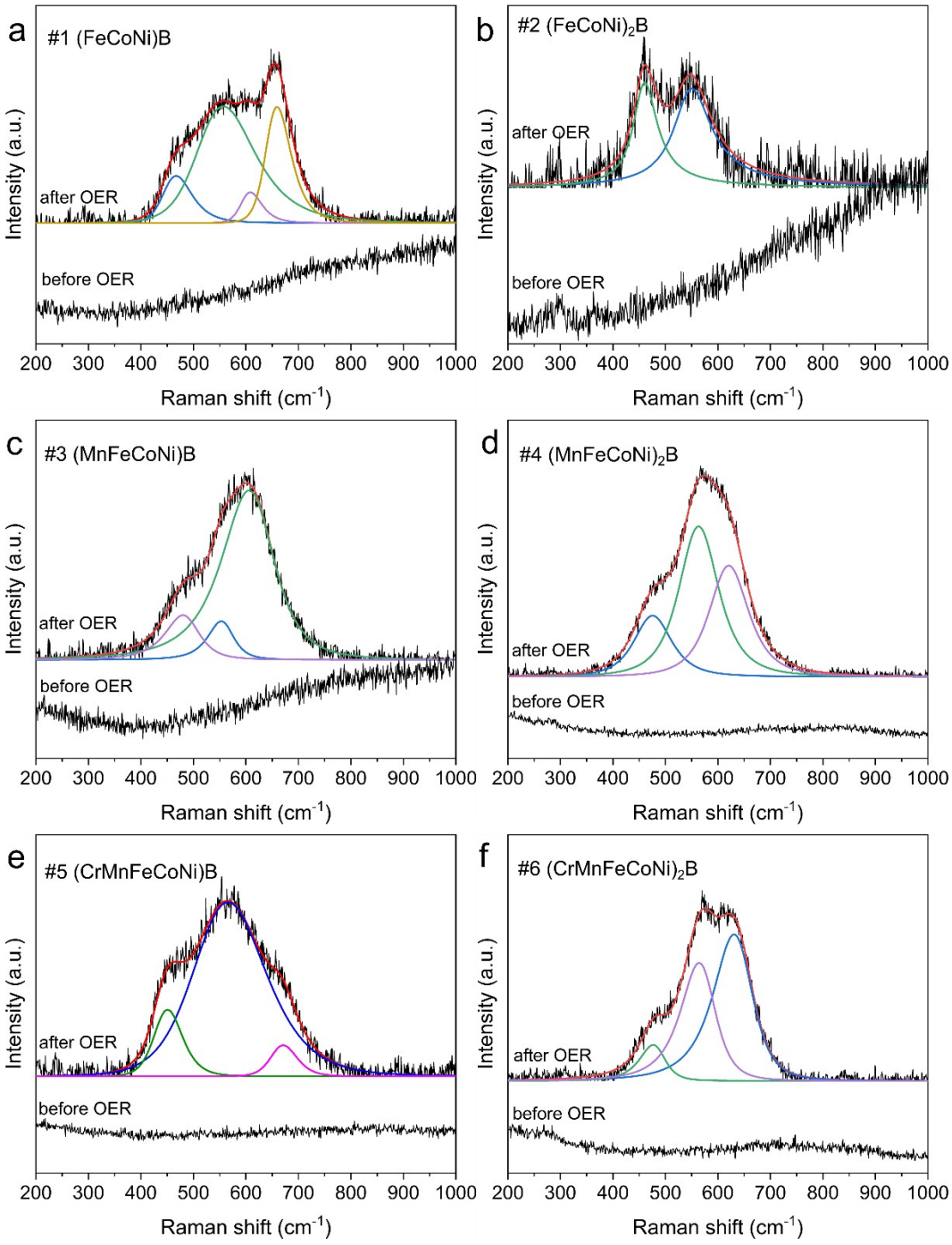

Figure S14. Raman spectra of the MEB/HEB catalysts before and after OER. Raman spectra of (FeCoNi)B (a), $(FeCoNi)_2B$ (b), (MnFeCoNi)B (c), $(MnFeCoNi)_2B$ (d), (CrMnFeCoNi)B (e), and

$(CrMnFeCoNi)_2B$ (f).

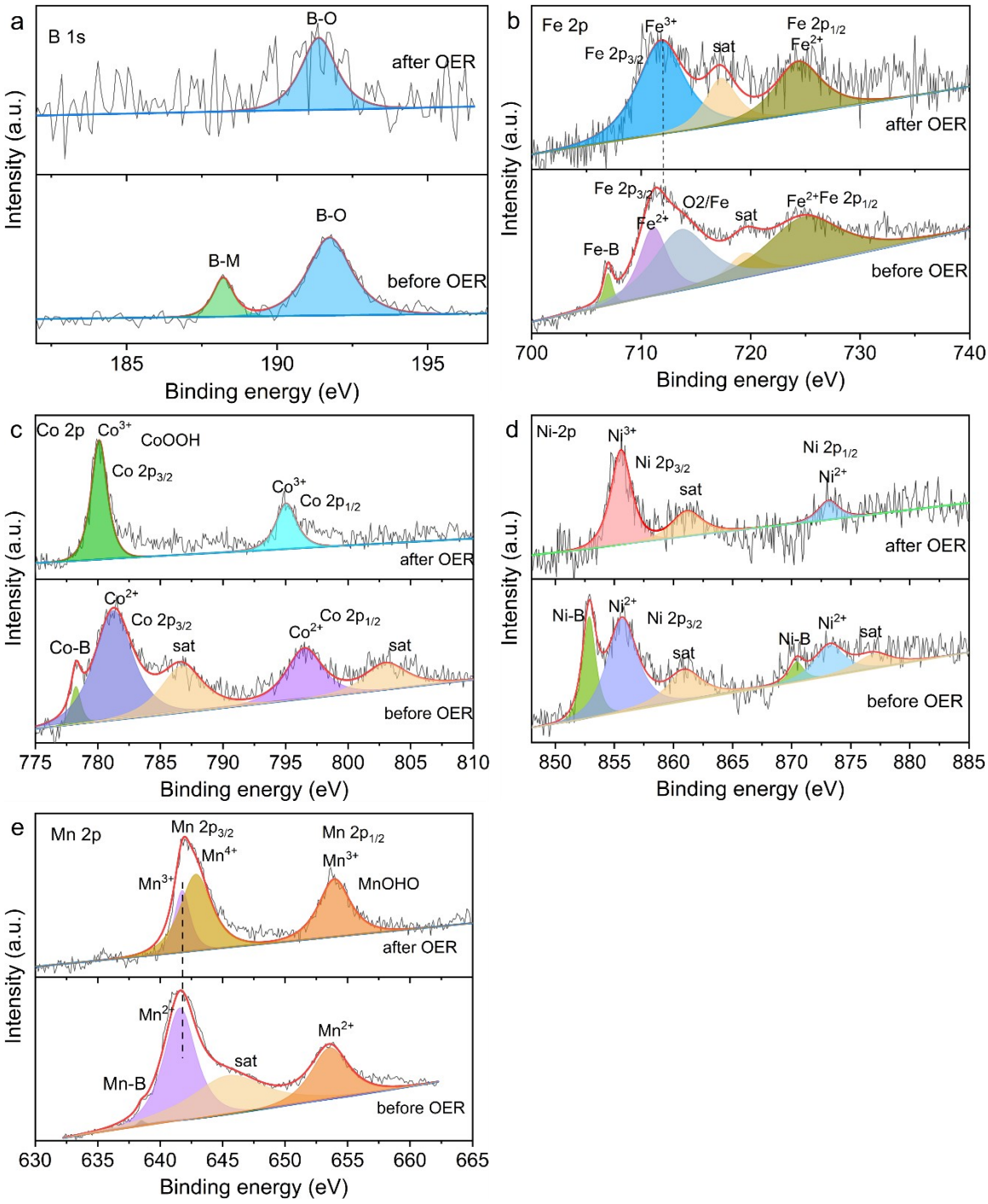

Figure S15. XPS spectra of $(MnFeCoNi)_2B$ (#4) before and after OER. XPS spectra of B 1s (a),

Fe 2p (b), Co 2p (c), Ni 2p (d) and Mn 2p (e).

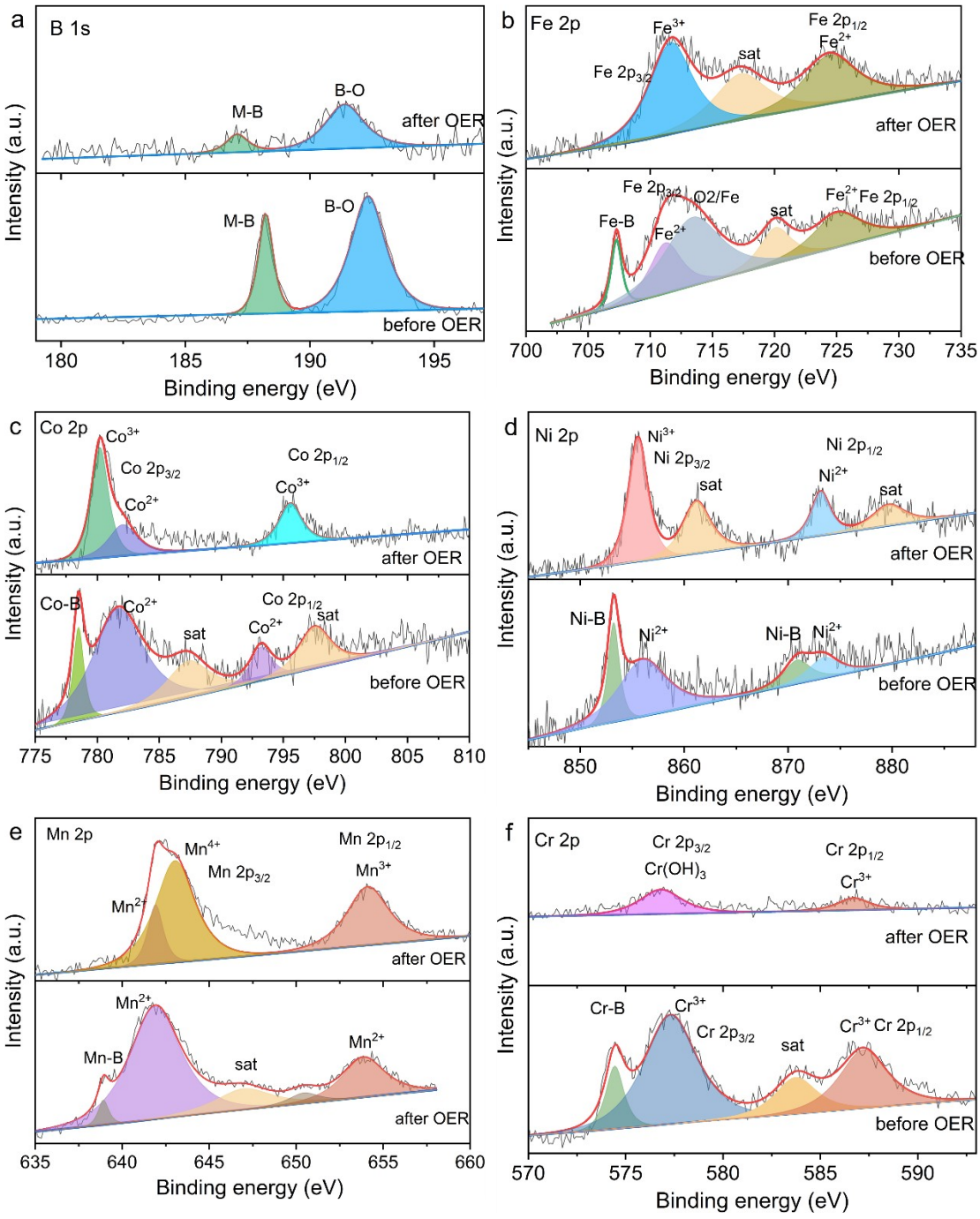

Figure S16. XPS spectra of (CrMnFeCoNi)B (#5) before and after OER. XPS Spectra of B 1s (a), Cr 2p (b), Mn 2p (c), Fe 2p (d), Co 2p (e), and Ni 2p (f).

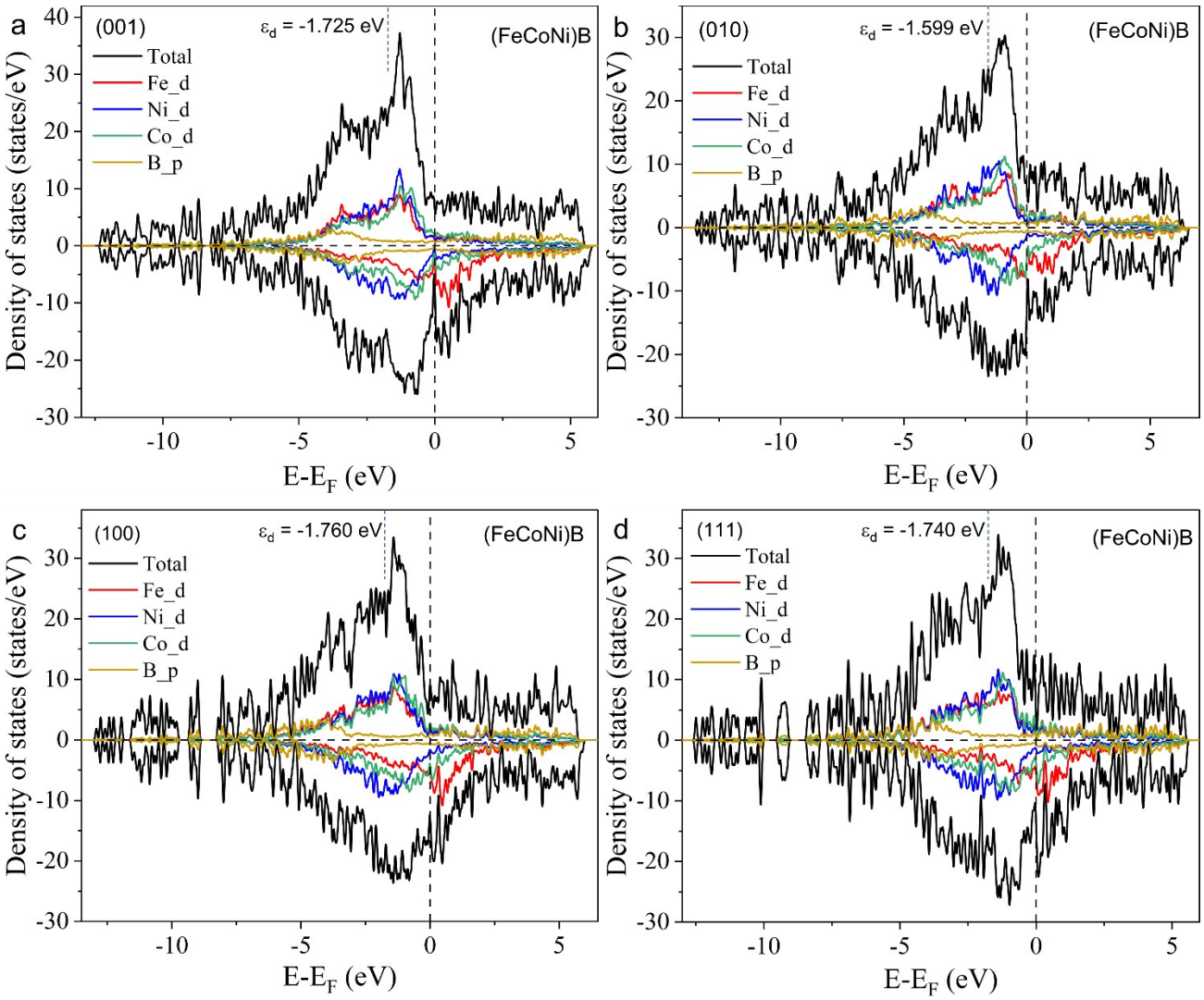

Figure S17. DFT-calculated surface electronic structures of (FeCoNi)B. The d-band DOS of the (001) (a), (010) (b), (100) (c), and (111) (d) surfaces of (FeCoNi)B (#1). The spin-up and spin-down DOS are depicted using the positive and negative values, respectively.

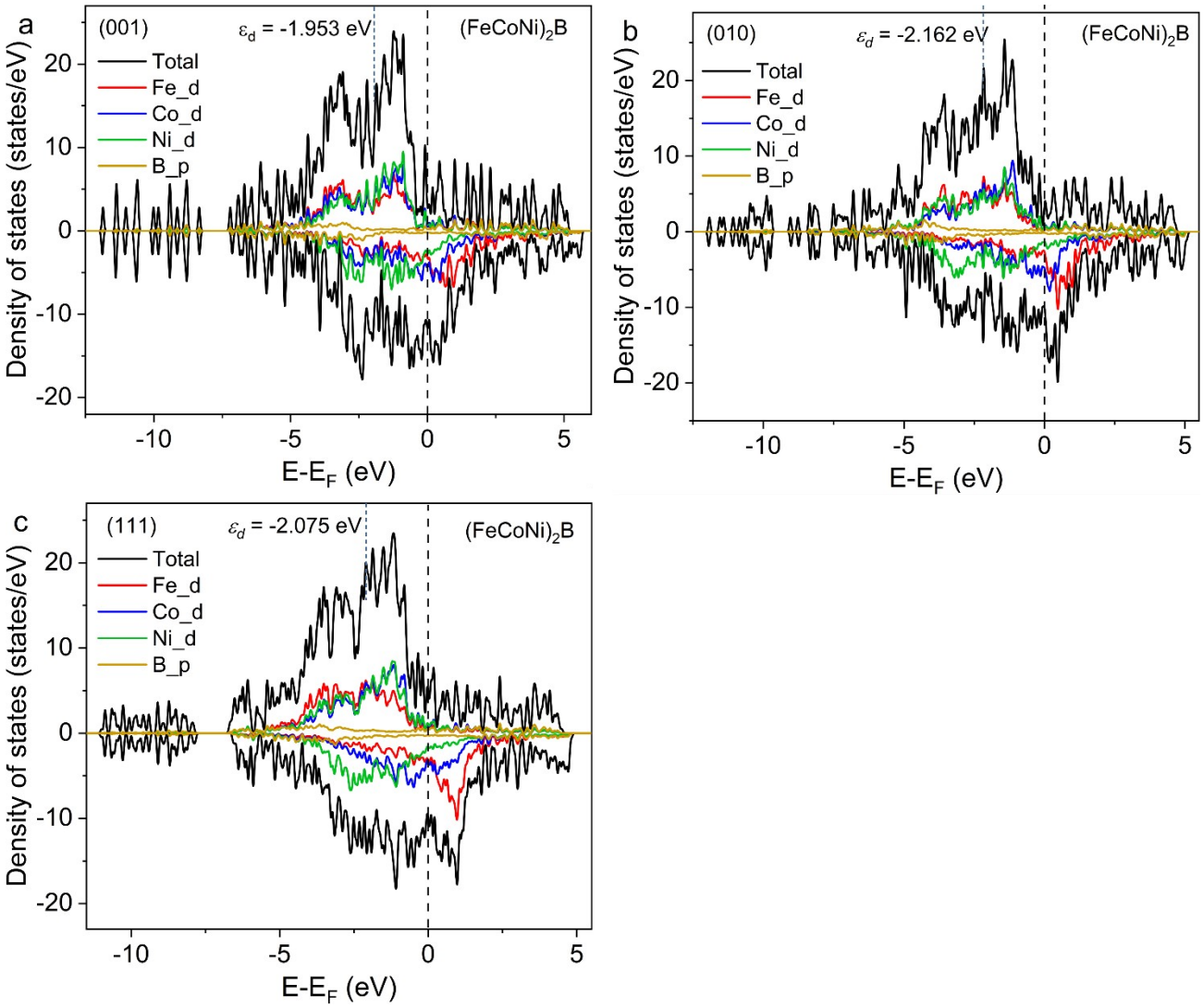

Figure S18. DFT-calculated surface electronic structures of $(FeCoNi)_2B$. The d-band DOS of the (001) (a), (010) (b), and (111) (c) surfaces of $(FeCoNi)_2B$ (#2). The spin-up and spin-down DOS are depicted using the positive and negative values, respectively.

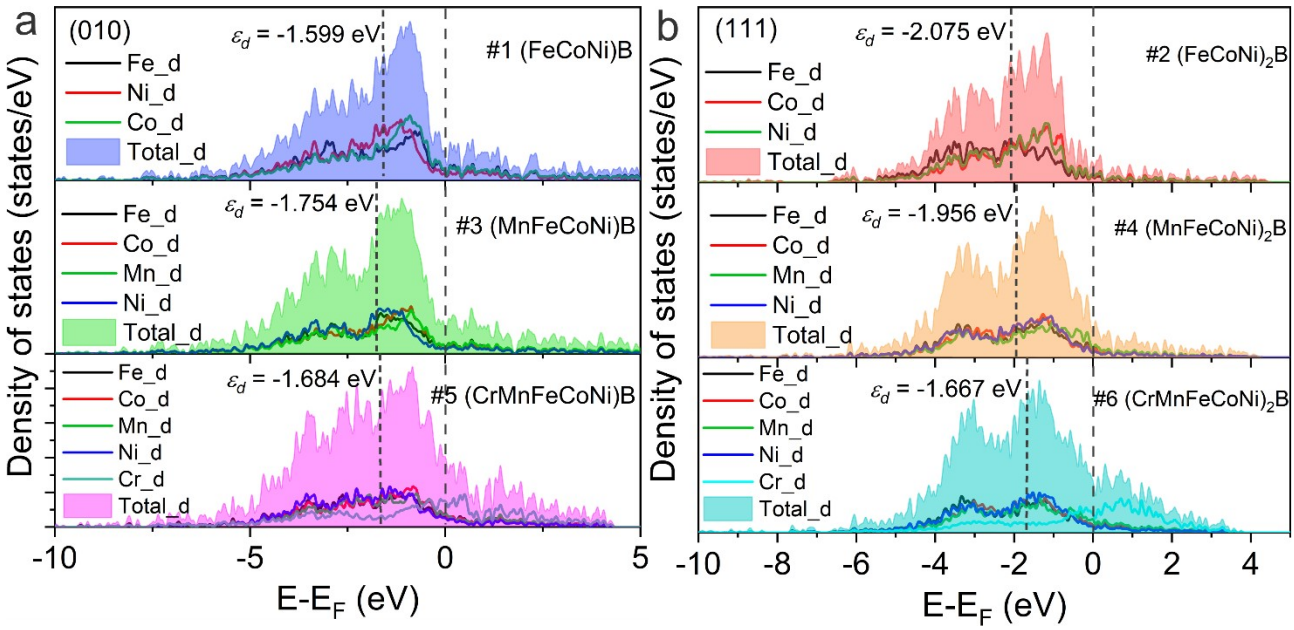

Figure S19. DFT-calculated spin-up DOS and d-band centers of specified surfaces of the MEB/HEB catalysts. (a), The d-band DOS and centers of the (010) surfaces of (FeCoNi)B (#1), (MnFeCoNi)B (#3), and (CrMnFeCoNi)B (#5). (b), The d-band DOS and centers of the (111) surfaces of (FeCoNi)$_2$B (#2), (MnFeCoNi)$_2$B (#4), and (CrMnFeCoNi)$_2$B (#6).

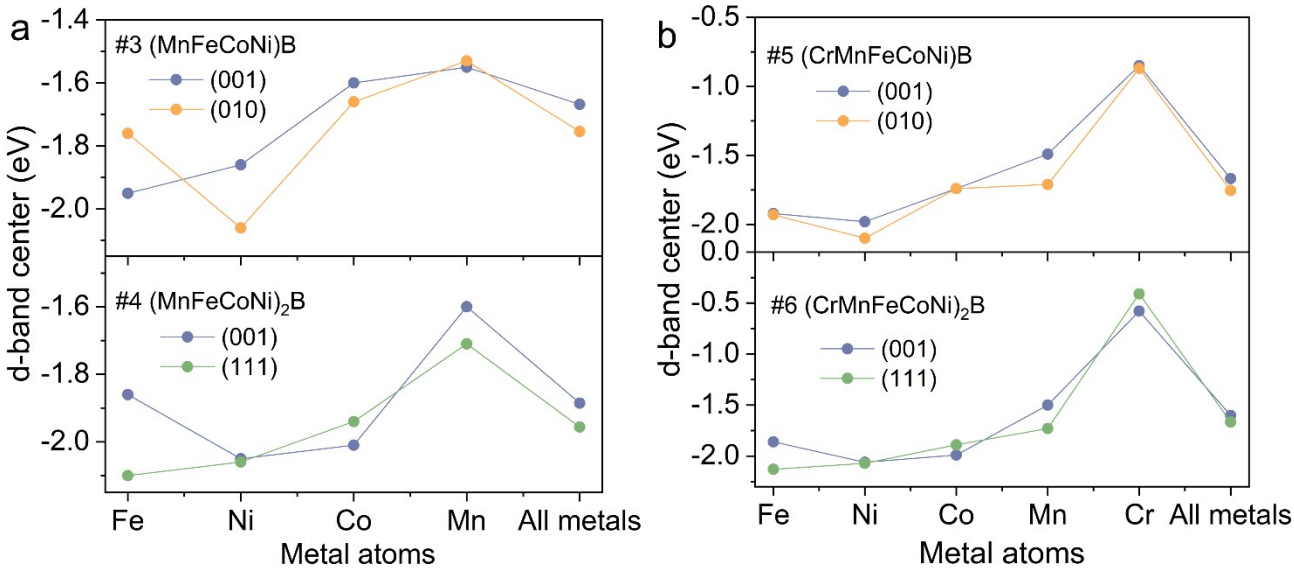

Figure S20. The calculated surface d-band centers of the MEB/HEB catalysts: The d-band centers

of Fe, Ni, Co, Mn and/or Cr, and all metals distributed on the (001) and (010) / (111) surfaces of (MnFeCoNi)B (#3) (a), $(MnFeCoNi)_2B$ (#4) (a), (CrMnFeCoNi)B (#5) (b), and $(CrMnFeCoNi)_2B$ (#6) (b).

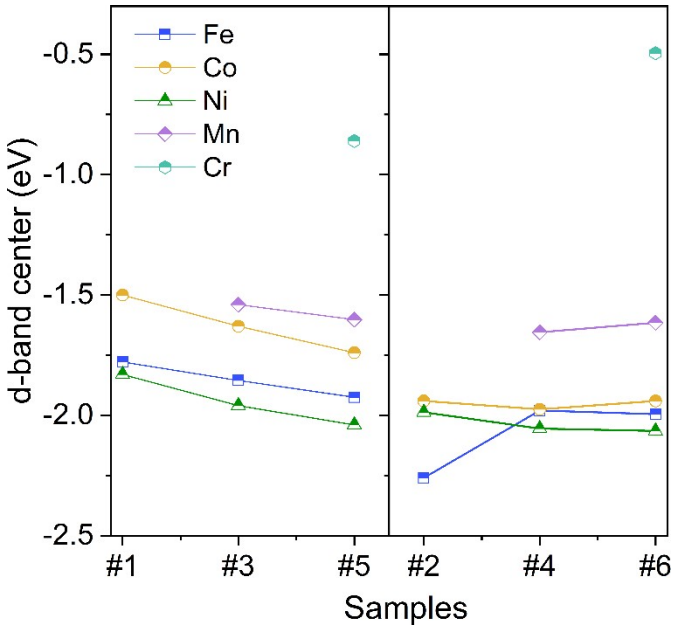

Figure S21. The averaged surface d-band centers of the MEB/HEB catalysts. The d-band centers of Fe, Co, Ni, Mn, and/or Cr in #1 – #6 catalysts, where the d-band center is the average of the centers of the (001), (010), (100) (#1 only), and (111) (#1 only) surfaces of the MB-type borides (#1, #3, and #5), or the average of the centers of the (001), (010) (#2 only), and (111) surfaces of the M_2B-type borides (#2, #4, and #6).

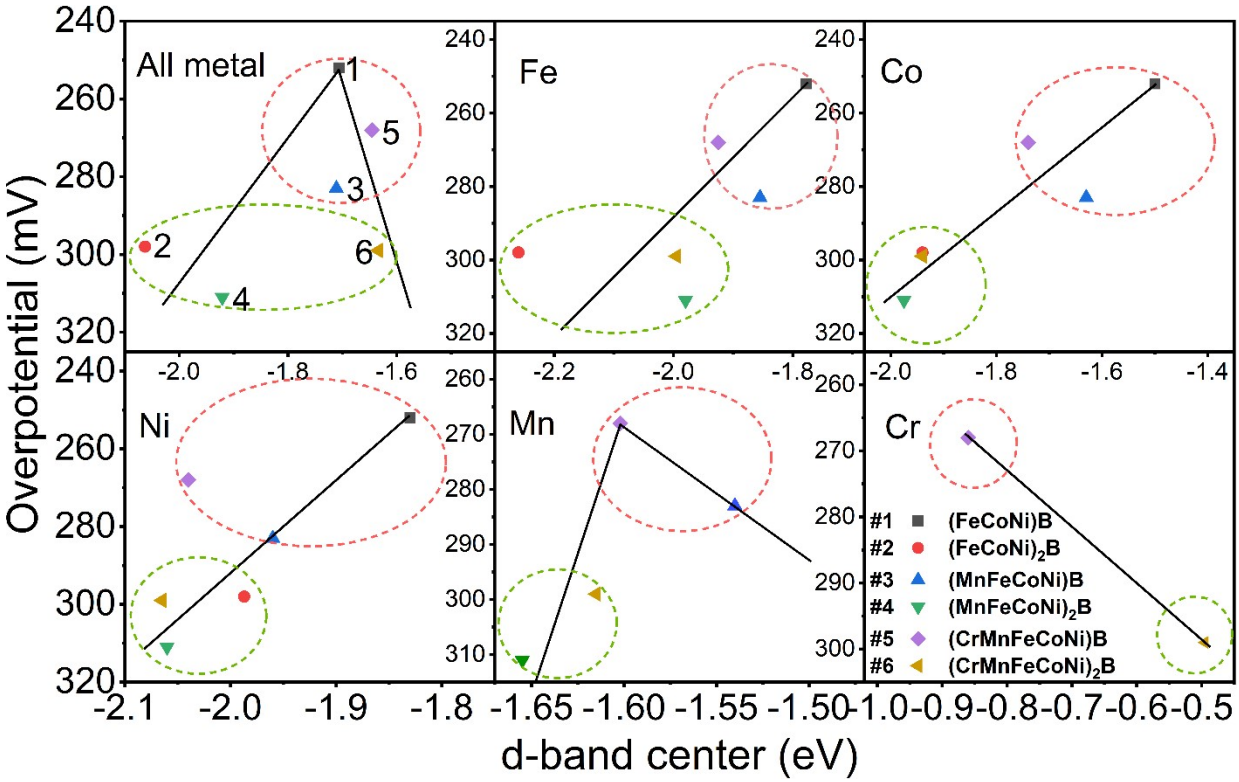

Figure S22. The relationships between the experimental overpotentials and the d-band centers of Fe, Co, Ni, Mn and/or Cr, and all metals, where the centers are the surface-averaged values as defined in Figure S20. Red dashed lines enclose the MB-type borides, and the green dashed lines enclose the M_2B-type borides.

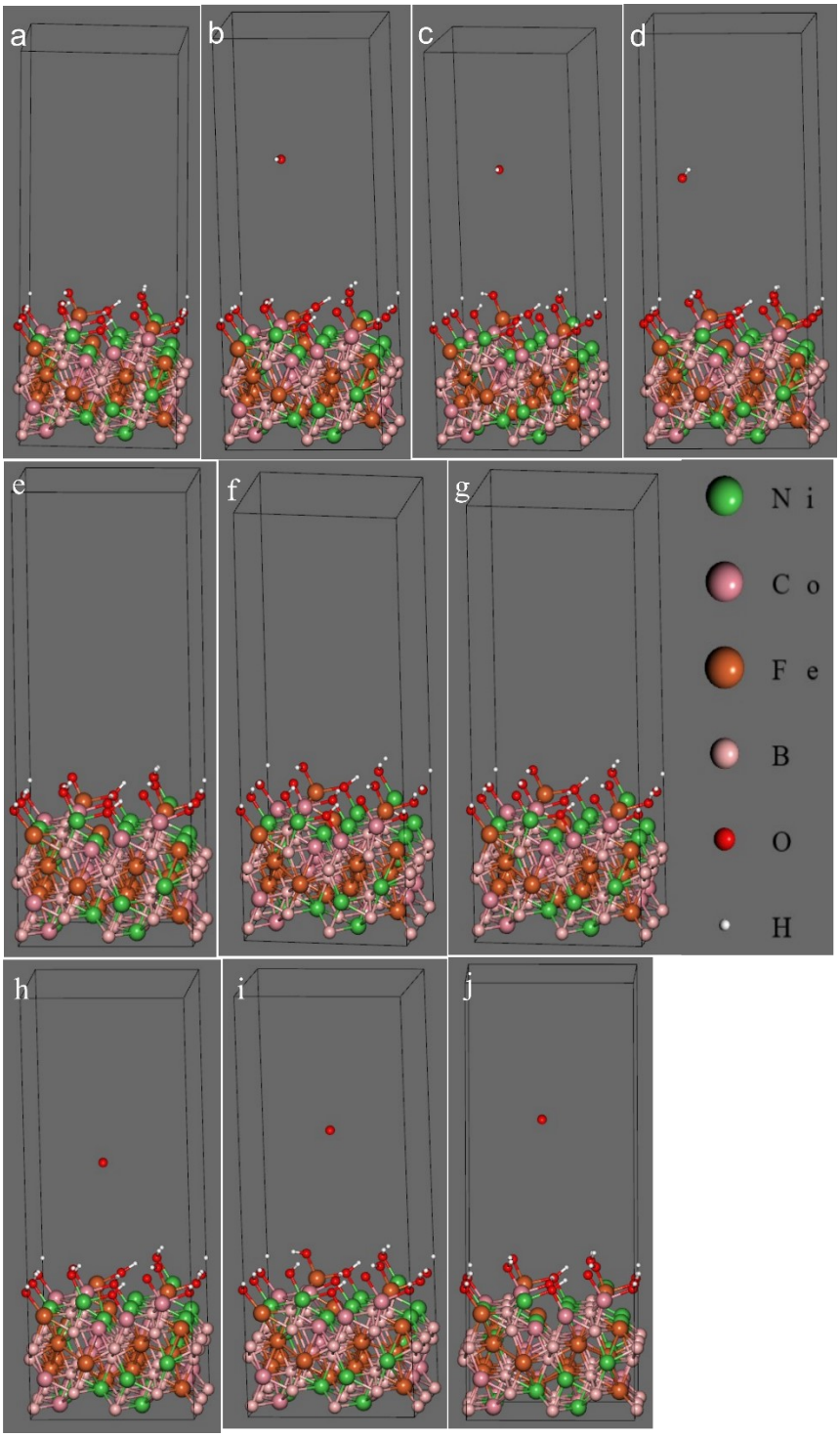

Figure S23. Atomic models of the hydroxylated (FeCoNi)B (100) surface showing the adsorption of OH / O intermediates on different cation (Fe, Co, Ni) sites. (a) The optimized (FeCoNi)B (100)

surface with 6 B atomics removed to expose 6 metal atoms, and with the surface cations fully hydroxylated by 12 adsorbed OH groups (6 standing OH groups and 6 bridging OH groups). (b-d) The optimized configuration of the surface after moving one OH group previously adsorbed on an Fe (b), Co (c), or Ni (d) site to a faraway distance, simulating the status before the OH adsorption; (e-g) The optimized configuration of the surface with one O anion adsorbed on an Fe (e), Co (f), or Ni (g) site while keeping all other metal sites hydroxylated; (h-j) The optimized configuration of the surface after moving one O anion previously adsorbed on an Fe (h), Co (i), or Ni (j) site to a faraway distance, simulating the status before the O adsorption. Atom color coding is shown in panel (g).

Table S1. The lattice parameters and unit cell volumes of the MEB/HEB catalysts derived from XRD data

Catalyst	***a*** **(Å)**	***Δa*** **(Å)**	***b*** **(Å)**	***Δb*** **(Å)**	***c*** **(Å)**	***Δc*** **(Å)**	***V*** **(Å^3)**	***ΔV*** **(Å^3)**
(FeCoNi)B	3.9918	0.0001	5.384	0.0002	2.9914	0.0001	64.453	0.007
$(FeCoNi)_2B$	5.0527	0.0002			4.2271	0.0003	107.120	0.010
(MnFeCoNi)B	4.0284	0.0020	5.4558	0.0020	2.9717	0.0001	65.315	0.007
$(MnFeCoNi)_2B$	5.0858	0.0001			4.2301	0.0002	109.419	0.010
(CrMnFeCoNi)B	4.0765	0.0001	5.5088	0.0002	2.9482	0.0003	66.196	0.007
$(CrMnFeCoNi)_2B$	5.1477	0.0004			4.2498	0.0004	112.616	0.020

Table S2. The C_{dl} and ECSA of the MEB/HEB catalysts and the IrO_2 benchmark

No.	Catalyst	C_{dl} (mF/cm^2)	ECSA (cm^2)
#1	(FeCoNi)B	2.90	72.5
#2	$(FeCoNi)_2B$	0.60	15.0
#3	(MnFeCoNi)B	2.80	70.0
#4	$(MnFeCoNi)_2B$	1.10	27.5
#5	(CrMnFeCoNi)B	2.55	63.8
#6	$(CrMnFeCoNi)_2B$	0.55	13.8
#7	IrO_2	35.6	890.0

Table S3. Comparison of the OER performance of the MEB/HEB catalysts in this work with recently reported boride catalysts in alkaline electrolyte (NF = Nickel foam, CF = Carbon fiber, and GC = Glassy carbon)

Catalysts	Synthesis methods	Substrate	Overpotential (mV) (at 10 mA cm^{-2})	Tafel Slop (mV dec^{-1})	Reference
(FeCoNi)B (#1)	spark plasma sintering	NF	219 [a]	23.9 [a]	This work
(CrMnFeCoNi)B (#5)	spark plasma sintering	NF	250	27.7	This work

IrO_2	Commercial	NF	299	56.8	This work
Ni_xB	Chemical reduction and anneal	NF	284	89	[1]
Co_2B	Ball-milling	CF	287	50.7	[2]
FeB_2	Chemical reduction and anneal	GC	296	52.4	[3]
Co-10Ni-B	Chemical reduction	GC	330	73.3	[4]
FeNiB-700	Solid-phase boronation reaction	-	272	89.2	[5]
NiFe-Boride	Chemical reduction	NF	167	25	[6]
$FeCoB_2$	Chemical reduction	GC	295	84	[7]
Fe-Co-2.3Ni-B	Chemical reduction	GC	274	38	[8]
NiCoFeB	Chemical reduction	GC	284	98	[9]
FeCoNiSiB	melt	-	230	85	[10]

	spinning				
CoFeNiMnZnB	Chemical reduction	NF	261	56.8	[11]

[a] In fact, the overpotential (at 10 mA cm^{-2}) of our #1 catalyst is lower than those of 365 out of 376 reported catalysts (as summarized in the review articles[12-17]), and the Tafel slope of the #1 catalyst is lower than those of 375 out of 376 reported catalysts (as summarized in the review articles[12-17]). In particular, our #1 catalyst is the second topmost OER catalyst among ~ 390 reported catalysts (including those cited in this Table and those summarized in Refs. [12-17]) in terms of having both a low overpotential (at 10 mA cm^{-2}) and a low Tafel slope.

Table S4. Kinetic parameters obtained from fitting of OER polarization curves using equation S7 (for elementary reaction S2 being the rate-determining-step)

Sample No.	**Catalyst**	**α_2**	**k_2^0 (mA/cm²)**
#1	(FeCoNi)B	0.60	3.12×10^{-6}
#2	$(FeCoNi)_2B$	0.53	1.17×10^{-6}
#3	(MnFeCoNi)B	0.62	3.75×10^{-7}
#4	$(MnFeCoNi)_2B$	0.51	1.51×10^{-7}
#5	(CrMnFeCoNi)B	0.54	1.86×10^{-6}
#6	$(CrMnFeCoNi)_2B$	0.66	1.38×10^{-6}

α_i: electron transfer coefficient and k_i^0 : standard rate constant.

Table S5. The fitted Raman peaks of the MEB/HEB catalysts after OER

No.	Catalyst	Centers of Raman peaks (cm^{-1})
#1	(FeCoNi)B	467, 556, 608, 659
#2	$(FeCoNi)_2B$	460, 550
#3	(MnFeCoNi)B	480, 553, 605
#4	$(MnFeCoNi)_2B$	475, 563, 620
#5	(CrMnFeCoNi)B	450, 566, 671
#6	$(CrMnFeCoNi)_2B$	476, 564, 630

Table S6. The DFT-predicted lattice parameters of the six MEB/HEB catalysts under study

No.	Catalyst	*a* (Å)	*b* (Å)	*c* (Å)	*V* ($Å^3$)
#1	(FeCoNi)B	4.0491	5.5630	2.9425	66.280
#2	$(FeCoNi)_2B$	5.0385		4.2184	107.297
#3	(MnFeCoNi)B	4.0274	5.0249	3.2776	68.644
#4	$(MnFeCoNi)_2B$	5.0697		4.2322	108.710
#5	(CrMnFeCoNi)B	4.1061	5.6355	2.9613	66.520
#6	$(CrMnFeCoNi)_2B$	5.0856		4.2489	109.856

Supplementary Note

Microkinetic Equations of OER.

The elementary reactions in an OER in an alkaline condition include

$M^* + OH^- \rightleftharpoons M\text{-}OH^* + e^-$ (Step 1)

$M\text{-}OH^* + OH^- \rightleftharpoons M\text{-}O^* + e^- + H_2O$ (Step 2)

$M\text{-}O^* + OH^- \rightleftharpoons M\text{-}OOH^* + e^-$ (Step 3)

$M\text{-}OOH^* + OH^- \rightleftharpoons M\text{-}OO^{-}* + H_2O$ (Step 4)

$M\text{-}OO^{-}* \rightleftharpoons M^* + e^- + O_2$ (Step 5)

where M denotes a site on a catalyst surface. On the basis of the above OER mechanism, Shinagawa et al.[18] derived various microkinetic equations of OER. If reaction S1 is the rate determining step, the overall kinetic rate equation is:

$$I = nFAk_1^0 a_{OH^-} exp\{(1-\alpha_1)\, f\eta_1\} \quad \text{(Equation S1)}$$

If reaction S2 is the rate determining step, the overall kinetic rate equation is:

$$I = nFA\frac{K_1^0\, k_2^0 exp(f\eta_1) a_{OH^-}^{\ 2} exp\{(1-\ \alpha_2)\, f\eta_2\}}{K_1^0 exp(f\eta_1) a_{OH^-} + 1} \quad \text{(Equation S2)}$$

If reaction S3 is the rate determining step, the overall kinetic rate equation is:

$$I = nFA\frac{K_1^0 K_2^0 exp\{(\eta_1+\eta_2)\, f\}\, k_3^0 exp\{(1-\ \alpha_3)\, f\eta_3\} a_{OH^-}^{\ 3}}{a_{H_2O} + K_1^0 exp(f\eta_1) a_{OH^-} a_{H_2O} + K_1^0 K_2^0 exp\{(\eta_1+\eta_2)\, f\} a_{OH^-}^{\ 2}} \quad \text{(Equation S3)}$$

If reaction S4 is the rate determining step, the overall kinetic rate equation is:

$$I = nFAk_4^0 a_{OH^-} \theta_3$$ (Equation S4)

If reaction S5 is the rate determining step, the overall kinetic rate equation is

$$I = nFAk_5^0 a_{OH^-} exp\{(1 - \alpha_5) f\eta_5\}\theta_4$$ (Equation S5)

For a detailed description of the involved variables, the derivation of above equations, and the procedure for fitting the polarization curves using above equations, please refer to refs.[18, 19]

References

1. Masa, J.; Sinev, I.; Mistry, H.; Ventosa, E.; De La Mata, M.; Arbiol, J.; Muhler, M.; Roldan Cuenya, B.; Schuhmann, W. Ultrathin high surface area nickel boride (Ni_xB) nanosheets as highly efficient electrocatalyst for oxygen evolution. *Adv. Energy Mater.* **2017**, *7*, 1700381.

2. Ma, X.; Wen, J.; Zhang, S.; Yuan, H.; Li, K.; Yan, F.; Zhang, X.; Chen, Y., Crystal Co_xB (x= 1–3) synthesized by a ball-milling method as high-performance electrocatalysts for the oxygen evolution reaction. *ACS Sustainable Chem. Eng.* **2017**, *5*, 10266-10274.

3. Li, H.; Wen, P.; Li, Q.; Dun, C.; Xing, J.; Lu, C.; Adhikari, S.; Jiang, L.; Carroll, D. L.; Geyer, S. M. Retracted: Earth-Abundant Iron Diboride (FeB2) Nanoparticles as Highly Active Bifunctional Electrocatalysts for Overall Water Splitting. *Adv. Energy Mater.* **2017**, *7*, 1700513.

4. Zhang, J.; Li, X.; Liu, Y.; Zeng, Z.; Cheng, X.; Wang, Y.; Tu, W.; Pan, M. Bi-metallic boride electrocatalysts with enhanced activity for the oxygen evolution reaction. *Nanoscale* **2018**, *10*, 11997-12002.

5. Yuan, H.; Wang, S.; Gu, X.; Tang, B.; Li, J.; Wang, X. One-step solid-phase boronation to fabricate self-supported porous FeNiB/FeNi foam for efficient electrocatalytic oxygen evolution and overall water splitting. *J. Mater. Chem. A* **2019**, *7*, 19554-19564.

6. Wang, N.; Xu, A.; Ou, P.; Hung, S. F.; Ozden, A.; Lu, Y. R.; Abed, J.; Wang, Z.; Yan, Y.; Sun, M. J. Boride-derived oxygen-evolution catalysts. *Nat. Commun.* **2021**, *12*, 6089.

7. Zou, X.; Zhang, W.; Zhou, X.; Song, K.; Ge, X.; Zheng, W. The surface of metal boride tinted by oxygen evolution reaction for enhanced water electrolysis. *J. Energy Chem.***2022**, *72*, 509-515.

8. Nsanzimana, J. M. V.; Peng, Y.; Xu, Y. Y.; Thia, L.; Wang, C.; Xia, B. Y.; Wang, X. An efficient and earth-abundant oxygen-evolving electrocatalyst based on amorphous metal borides. *Adv. Energy Mater.* **2018**, *8*, 1701475.

9. Li, Y.; Huang, B.; Sun, Y.; Luo, M.; Yang, Y.; Qin, Y.; Wang, L.; Li, C.; Lv, F.; Zhang, W. Multimetal borides nanochains as efficient electrocatalysts for overall water splitting. *Small* **2019**, *15*, 1804212.

10. Wang, H.; Wei, R.; Li, X.; Ma, X.; Hao, X.; Guan, G. Nanostructured amorphous $Fe_{29}Co_{27}Ni_{23}Si_9B_{12}$ high-entropy-alloy: an efficient electrocatalyst for oxygen evolution reaction. *J. Mater. Sci. Technol.* **2021**, *68*, 191-198.

11. Wang, X.; Zuo, Y.; Horta, S.; He, R.; Yang, L.; Ostovari Moghaddam, A.; Ibáñez, M.; Qi, X.; Cabot, A. CoFeNiMnZnB as a high-entropy metal boride to boost the oxygen evolution reaction. *ACS Appl. Mater. Interfaces* **2022**, *14*, 48212-48219.

12. Olowoyo, J. O.; Kriek, R. J., Recent progress on bimetallic-based spinels as electrocatalysts for the oxygen evolution reaction. *Small* **2022**, *18*, 2203125.

13. Tahir, M.; Pan, L.; Idrees, F.; Zhang, X.; Wang, L.; Zou, J.-J.; Wang, Z. L., Electrocatalytic oxygen evolution reaction for energy conversion and storage: A comprehensive review. *Nano Energy* **2017**, *37*, 136-157.

14. Han, L.; Dong, S.; Wang, E., Transition-metal (Co, Ni, and Fe)-based electrocatalysts for the water oxidation reaction. *Adv. mater.* **2016**, *28*, 9266-9291.

15. Suen, N. T.; Hung, S.-F.; Quan, Q.; Zhang, N.; Xu, Y. J.; Chen, H. M. Electrocatalysis for the oxygen evolution reaction: recent development and future perspectives. *Chem. Soc. Rev.* **2017**, *46*, 337-365.

16. Cui, L.; Zhang, W.; Zheng, R.; Liu, J. Electrocatalysts based on transition metal borides and borates for the oxygen evolution reaction. *Chem. Eur. J.* **2020**, *26*, 11661-11672.

17. Yao, Y.; Zhang, Z.; Jiao, L. Development strategies in transition metal borides for electrochemical water splitting. *Energy Environ. Mater.* **2022**, *5*, 470-485.

18. Shinagawa, T.; Garcia-Esparza, A. T.; Takanabe, K. Insight on Tafel slopes from a microkinetic analysis of aqueous electrocatalysis for energy conversion. *Sci. Rep.* **2015**, *5*, 13801.

19. Li, W.; Li, C.; Dong, H.; Zhang, X.; Liu, J.; Song, M.; Wang, G.; Zhao, L.; Sheng, H.; Chen, B. Expediting oxygen evolution by optimizing cation and anion complexity in electrocatalysts based on metal phosphorous trichalcogenides. *Angew. Chem. Int. Ed.* **2023**, *135*, e202214570.